

Evidence for the Full Hard X-ray Spectral Signature of Nonuniform Ionization in a Solar Flare

Yang Su^{1,2,3}

`yang.su@nasa.gov`

Gordon D. Holman²

`gordon.d.holman@nasa.gov`

and

Brian R. Dennis²

ABSTRACT

The hard X-ray (HXR) emission from solar flares is observed primarily from the footpoints of flare magnetic loops, where nonthermal electrons are understood to emit thick-target bremsstrahlung as they stream from the fully-ionized hot corona to the denser, cooler, and partially ionized chromosphere. The change in the plasma ionization along the path of the electrons should result in a characteristic upward break and corresponding flattening of the X-ray spectrum with increasing energy at lower energies, and a downward break at higher energies. Due to the presence of thermal emission, the upward break usually cannot be observed.

We report the first evidence for both breaks in spectra measured with the Reuven Ramaty High Energy Solar Spectroscopic Imager (RHESSI) during the GOES X1.2 class flare that happened on 31 October 2002. The RHESSI X-ray spectral analysis shows both the break-up at ~ 49 keV and the break-down at ~ 134 keV at the HXR peak time. The time evolution of both breaks also agrees with the nonuniform ionization model. Other possible explanations for the breaks are considered, but the nonuniform ionization model (NUI) provides the simplest explanation for the spectral shape and its time evolution.

¹Department of Physics, the Catholic University of America, Washington, DC 20064

²NASA Goddard Space Flight Center, Solar Physics Laboratory, Code 671, Greenbelt, MD 20771

³Key Laboratory of Dark Matter and Space Astronomy, Purple Mountain Observatory, Chinese Academy of Sciences, Nanjing, China, 210008

We find that the average column density of the fully ionized plasma changed from $2 \times 10^{19} \text{ cm}^{-2}$ in the rise phase to $7 \times 10^{21} \text{ cm}^{-2}$ after the peak. This indicates that plasma in the target was heated and became ionized during the flare, in agreement with heating by the nonthermal electrons and chromospheric evaporation expected in the collisional thick-target model.

Subject headings: Sun: flares — Sun: X-rays, gamma rays — Sun: chromosphere

1. Introduction

It is believed that electrons are accelerated in the corona during a solar flare and then propagate along the legs of magnetic loops to the lower atmosphere. As the electrons lose energy due to Coulomb collisions, they also produce thick-target bremsstrahlung emission (Brown 1971). The basic collisional thick-target model assumes that the electrons lose all their energy in a cold, fully ionized target. However, in reality, high energy electrons can penetrate deep into the atmosphere where it is cooler and un-ionized. Therefore, the nonuniform ionization (NUI) thick-target model (Brown 1973; Emslie 1978; Kontar et al. 2002; Su et al. 2009) includes a region below the fully ionized plasma where the plasma is un-ionized. Because of the shielding effect of the proton, the Coulomb energy loss rate of nonthermal electrons is a factor of about 2.8 (for pure hydrogen) times lower in neutral material than in fully ionized plasma. On the other hand, the bremsstrahlung cross section is not affected by the ionization level. Therefore, the X-ray emission from electrons traversing this un-ionized region is enhanced by a factor of about 2.8 (see Figure 1) over that for an ionized region. As a result, the X-ray spectrum from a nonuniform ionization target (assuming that the injected electron distribution is a single-power-law) has both a break-up (i.e., the spectrum becomes harder, the spectral index becomes smaller) with increasing photon energy at low energies and a break-down (i.e., the spectrum becomes softer, the spectral index becomes larger) with increasing photon energy at high energies.

Due to the presence at low energies of bremsstrahlung from thermal plasma, the break-up feature usually cannot be observed. Taking a power-law electron flux distribution, $f(E_e) \propto E_e^{-\delta}$, with a power-law index δ of 4, for example, one will get a photon spectrum with a break-up feature at $\sim 6 \text{ keV}$ (Su et al. 2009) when the electrons enter a thick target where the plasma changes from fully ionized plasma to fully un-ionized plasma at a column density of $N_* = 1.2 \times 10^{20} \text{ cm}^{-2}$. However, if the column density N_* is high enough and/or the spectrum is relatively steep, it is possible that the break-up energy can be above the energy at which the thermal emission dominates over nonthermal emission. Kontar et al. (2002, 2003) used the nonuniform ionization model to fit spectra of several flares. However,

it is not clear that the spectra had the shape as expected from NUI, since the N_* they found was less than $5 \times 10^{20} \text{ cm}^{-2}$ (the electron energy required to reach this column density is less than 58 keV), and the spectra they fitted showed only the downward break.

We report the first evidence for the full spectrum showing both breaks expected from nonuniform ionization in the thick-target region. The GOES X1.2 class flare, observed by the Reuven Ramaty High Energy Solar Spectroscopic Imager (RHESSI, Lin et al. 2002; Smith et al. 2002) peaked at 16:51:08 UT on 31 October 2002 in hard X-rays above 50 keV. Other possible explanations for the spectral shape are also considered, but NUI is found to provide the simplest explanation overall.

2. Nonuniform Ionization Model

Here we ignore magnetic mirroring, directivity of the emission, the electron pitch-angle distribution, and pitch-angle scattering of the electrons, as did Brown et al. (1998) and Kontar et al. (2002). We do, however, include relativistic effects in the energy loss rate. When a beam of nonthermal electrons is injected into a thick target with a nonuniform distribution of fractional ionization level $x(N)$, N being the column density, the energy loss rate of nonthermal electrons due to Coulomb collisions can be written as

$$\frac{dE}{dt} = \frac{-4\pi r_0^2 n c \Lambda m_e c^2}{\beta} (\lambda + x(N)), \quad (1)$$

where $r_0 = e^2/(m_e c^2)$ is the classical electron radius, e is electron charge, m_e is the electron rest mass, n is the number density of target electrons, $\beta = v/c$ is ratio of the electron speed to the speed of light, $\Lambda = \Lambda_{ee} - \Lambda_{eH} \simeq 17$, where Λ_{ee} and Λ_{eH} are the Coulomb logarithms for the collision of energetic electrons with thermal electrons and neutral hydrogen, respectively, and $\lambda = \Lambda_{eH}/\Lambda \simeq 0.55$ (Brown 1973). Although these logarithmic factors are not formally constant, they vary slowly and we take them to be constant, as did previous authors.

From Equation 1, the differential relation between N and E is

$$\frac{dN}{dE} = \frac{nv dt}{dE} = -\frac{m_e c^2}{4\pi e^4 \Lambda (\lambda + x(N))} \frac{(2m_e c^2 + E)}{(E + m_e c^2)^2} E. \quad (2)$$

We use a step-function ionization profile (Kontar et al. 2002; Su et al. 2009) which assumes that a pure hydrogen plasma is fully ionized above a given column density N_* (cm^{-2}) and fully un-ionized below, i.e., the fractional ionization $x(N)$ is given by the expression:

$$x(N) = \begin{cases} 1, & N < N_* \\ 0, & N > N_* \end{cases} \quad (3)$$

An effective column density M can be defined as (Brown et al. 1998)

$$M = \int_0^N (\lambda + x(N)) dN = \frac{1}{4\pi e^4 \Lambda} \left[\frac{m_e c^2}{E_0 + m_e c^2} E_0^2 - \frac{m_e c^2}{E + m_e c^2} E^2 \right]. \quad (4)$$

The last expression, where E_0 is the initial energy of an electron and E is the energy of the electron at depth M , is obtained by solving Equation 2.

By setting E to 0, one obtains the relation between N_* and E_* , the minimum initial electron energy required to reach the column density N_* :

$$N_* = \frac{1}{4\pi e^4 \Lambda (\lambda + 1)} E_*^2 \left(\frac{m_e c^2}{E_* + m_e c^2} \right) \simeq 1.5 \times 10^{17} E_*^2 \left(\frac{m_e c^2}{E_* + m_e c^2} \right). \quad (5)$$

This differs from the non-relativistic result by the factor $mc^2/(E_* + mc^2) = \gamma_*^{-1}$, where γ_* is the relativistic gamma factor for E_* .

The thick-target photon flux (photons $\text{s}^{-1} \text{cm}^{-2} \text{keV}^{-1}$) at the Earth, in consideration of relativistic effects, for the step ionization function is

$$\begin{aligned} I_{step}(\varepsilon) &= \frac{1}{4\pi(AU)^2} \int_{\varepsilon}^{\infty} f(E_e) \left[\int_{\varepsilon}^{E_e} \frac{Q(\varepsilon, E) nv}{-dE/dt} dE \right] dE_e \\ &= \frac{1}{4\pi(AU)^2} \frac{m_e c^2}{4\pi e^4 \Lambda} \int_{\varepsilon}^{\infty} f(E_e) \left[\int_{\varepsilon}^{E_e} \frac{Q(\varepsilon, E) \beta^2}{\lambda + x} dE \right] dE_e \\ &= \frac{1}{4\pi(AU)^2} \frac{m_e c^2}{4\pi e^4 \Lambda} \int_{\varepsilon}^{\infty} Q(\varepsilon, E) \beta^2 \left[\int_E^{\infty} \frac{f(E_e)}{\lambda + x} dE_e \right] dE \\ &= \frac{1}{4\pi(AU)^2} \frac{m_e c^2}{4\pi e^4 \Lambda} \int_{\varepsilon}^{\infty} Q(\varepsilon, E) \beta^2 \left[\int_E^{E_x} \frac{f(E_e)}{\lambda + 1} dE_e + \int_{E_x}^{\infty} \frac{f(E_e)}{\lambda} dE_e \right] dE, \end{aligned} \quad (6)$$

where AU is the distance from the Sun to the Earth (in cm), $Q(\varepsilon, E)$ is the bremsstrahlung cross-section from Haug (1997), which closely approximates the full relativistic cross-section of Bethe and Heitler (equation 3BN of Koch & Motz 1959), $f(E_e)$ is the injected electron flux distribution function (electrons $\text{s}^{-1} \text{keV}^{-1}$) and E_x is the initial electron energy of electrons that is required to have energy E left at the depth of N_* . E_x is determined from Equation 4 by the relation

$$M_* = \frac{1}{4\pi e^4 \Lambda} \left[\frac{m_e c^2}{E_* + m_e c^2} E_*^2 \right] = \frac{1}{4\pi e^4 \Lambda} \left[\frac{m_e c^2}{E_x + m_e c^2} E_x^2 - \frac{m_e c^2}{E + m_e c^2} E^2 \right] \quad (7)$$

Solving Equation 7 for E_x gives

$$\begin{aligned} E_x(E_*, E) &= \frac{E^2}{2(E + m_e c^2)} + \frac{E_*^2}{2(E_* + m_e c^2)} \\ &\quad + \sqrt{\left(\frac{E^2}{2(E + m_e c^2)} + \frac{E_*^2}{2(E_* + m_e c^2)} \right)^2 + \left(\frac{E^2}{E + m_e c^2} + \frac{E_*^2}{E_* + m_e c^2} \right) m_e c^2} \end{aligned} \quad (8)$$

Compared with $E_x = \sqrt{E^2 + E_*^2}$ for the non-relativistic case, this gives a maximum of $\sim 5\%$ difference in E_x for an E_* of 130 keV. Note that Su et al. (2009), as in this work, used the relativistic energy loss term in all calculations using the Haug cross-section, but did not use the relativistic relations between N and E derived here. Also note that Equation 4 of Su et al. (2009) was derived using the nonrelativistic energy loss term.

We use a single-power-law electron flux distribution function ($\text{s}^{-1} \text{ keV}^{-1}$) with a low-energy cutoff at E_c :

$$f(E_e) = (\delta - 1) \frac{\mathcal{F}_c}{E_c} \left[\frac{E_e}{E_c} \right]^{-\delta}, \quad (9)$$

where \mathcal{F}_c is the total electron flux above E_c , and δ is the power-law index of the electron distribution. E_c is taken to be 1 keV in this study so that it does not affect the spectral fits above 6 keV. For computational reason, a high-energy cutoff at 10 MeV was also included, which is high enough not to significantly affect the spectrum below 300 keV for the power-law indexes of interest here.

Figure 1 shows a comparison of the photon flux and spectral index γ versus photon energy ε for a fully ionized thick-target model and a NUI model with an injected electron distribution power-law index of $\delta = 4$. The spectral index γ for the fully ionized thick target (solid thin red line in bottom panel) varies with photon energy, with a change $\Delta\gamma < 0.2$, due to the use of the relativistic energy loss rate and the relativistic Haug cross-section (see also Holman 2003; Su et al. 2009). The spectral index γ of the photon spectrum from a NUI thick target is approximately the same as for the fully ionized thick target at low and high energies and is smaller around the electron break energy E_* (see the bottom panel of Figure 1), i.e., the spectrum is flattened around the break energy E_* , producing a valley in spectral index $\gamma(\varepsilon)$. The location of this valley depends on E_* and δ . The break-up and break-down features are located at the two sides of the valley. Usually the break-up part is buried by the thermal emission and therefore we cannot see it, even if it does exist in the emitted X-ray spectrum. However, the valley moves to a higher energy when E_* becomes larger and/or the electrons have a steeper power-law distribution (a larger δ), as does the break-up. Thus, the break-up feature can become visible at photon energies above those dominated by thermal bremsstrahlung, especially if the thermal emission is relatively weak.

3. The flare event

When the electrons have a steep power-law distribution, the photon spectrum is easily buried in the RHESSI instrumental background at high energies. Therefore, instead of looking for a steep photon spectrum, we looked for flares with large E_* from our previous paper

(Su et al. 2009). There we selected 20 flares and found that 15 of them had a downward break in their spectra. Of those 15 flares, 9 had spectra consistent with nonuniform ionization. The largest E_* was 107 keV for the flare on 31 October 2002 (flare No. 5 in Su et al. 2009).

Figure 2 shows the RHESSI and GOES light curves of this flare. The top panel shows the light curves in different energy bands for the entire flare while the middle panel is an enlarged plot around the peak time. The vertical lines in the middle panel indicate the six intervals used for spectral fitting. At 16:44 UT, a weak X-ray peak (interval 0 in the top plot) appeared before the X-class flare, accompanied by a small increase in the GOES flux. The Pixon image at 6-10 keV at this time is shown in the bottom left panel. Two coronal sources showed up first before the loop-like structure (middle image) appeared at the peak time (interval 4). The two sources at high energies were located at the footpoints (bottom right).

The HXR impulsive phase (above 50 keV) is short (~ 1 minute) for an X-class flare. We selected six 8-s time intervals around the peak time (from 31-Oct-2002 16:50:38.30 UT to 16:51:32.25 UT). Three of them (interval 1, 2, and 3) were in the A1 attenuator state and the other three (4, 5, and 6) in A3. The HXR peak (interval 4) occurred right after the attenuator change from A1 to A3. There are not enough HXR photon counts above 50 keV to confidently determine the spectral properties for the remaining time of the hard X-ray decay.

4. X-ray spectra

For all the X-ray spectral analysis, we used 1/3 keV energy bins from 3 to 15 keV, 1 keV bins between 15 and 50 keV, 3 keV bins between 50 to 80 keV, and 5 keV above 80 keV. Spectra were made for detector 1, 3, 4, 6, 8, and 9 individually so that we can apply the pulse pile-up correction and energy gain correction. This allows us to obtain 6 independent measurements of all spectral parameters to estimate uncertainties. An albedo photon correction (assuming isotropically emitted photons for the primary source, see Kontar et al. 2006; Kontar & Brown 2006) was also applied to all the spectra. The full RHESSI response matrix was used and the instrumental systematic uncertainty was set to zero for the spectral fits. In addition, to determine the uncertainties on the parameters, we obtained the 95% confidence intervals (~ 2 sigma) using a Monte Carlo method with 2000 iterations (the same method we used in Su et al. 2009).

We first used an isothermal component plus the nonuniform ionization model to fit

the spectra. A second isothermal component at a different temperature was added when needed. The reasons for this second component are: 1) It is required at low energies for a good spectral fit. 2) A secondary isothermal component might eliminate the break-up feature. Adding another isothermal component strengthens our conclusion if we still see the break-up in the spectra after including it. 3) We see evidence for a hotter thermal coronal source in the images at low energies. Caspi (2010) also found evidence for a spatially separated, high-temperature (over 30 MK) source in a flare.

The time evolution of E_* deduced from the spectral fits for each individual detector is shown in Figure 3. The 95% confidence intervals for E_* from detector 4 are also shown for comparison to the spread in the results from the different detectors. The average value of E_* obtained for the six time intervals are: 11, 32, 64, 108, 211 and 265 keV. The corresponding column densities N_* are: 2×10^{19} , 1.4×10^{20} , 5.5×10^{20} , 1.4×10^{21} , 4.7×10^{21} and $7 \times 10^{21} \text{ cm}^{-2}$. The intervals 1 and 6 have large uncertainties ($2^{+6}_{-1.9} \times 10^{19} \text{ cm}^{-2}$ and $7^{+275}_{-5} \times 10^{21} \text{ cm}^{-2}$, respectively) based on the scatter of the results from the different detectors and the 95% confidence intervals from detector 4, since the data do not show the full NUI spectrum and, thus, the parameters of the model cannot be well determined. At the peak times, however, the spectral shapes are well determined and the uncertainties in the derived parameters are relatively small. The increase of N_* with time indicates that more and more gas was heated up and became ionized during the HXR peak. The electron distribution index δ follows the usual soft-hard-soft evolution.

We also used a triple power-law to fit the spectra for the purpose of identifying the break-up and break-down in the spectra. Even though the spectral index γ of the spectrum from NUI changes continuously with energy (bottom panel of Figure 1), a triple power-law can still provide a good fit. The three indexes indicate whether or not the spectrum follows a steep-flat-steep variation from low energy to high energy. The two break energies give the approximate positions of the spectral breaks.

We now focus on intervals 3, 4 and 5, since they have relatively high count rates at high energies. Here we use detector 4 as a typical example. Figure 4 shows both the NUI fit and triple power-law fit to the spectra. The fit results and their uncertainties for the three intervals are shown in Table 1.

1) Interval 3, 31-Oct-2002 16:50:54.90 to 16:51:03.20 UT.

This interval is just before the peak. A single isothermal component was used for this interval (only the fit using detector 1 alone needed a second isothermal component). The best fit value of E_* at this time was 72 keV. However, the spectrum was relatively steep ($\delta = 4.64$) and the thermal emission only dominates below 12 keV. Therefore, the break-up is clearly visible. The triple power-law fit to the spectrum shows a break-up

with $\Delta\gamma_{21}=\gamma_2-\gamma_1 = -0.5$ at 30 keV and a break-down with $\Delta\gamma_{32}=\gamma_3-\gamma_2 = 0.37$ at 49 keV. Table 1 gives the uncertainties on the parameters. The break-up and break-down are still significant at the 95% confidence level.

- 2) Interval 4, 31-Oct-2002 16:51:07.35 to 16:51:15.65 UT.

The high value of $E_* = 125$ keV gives us a good opportunity to see the break-up and break-down features (see Figure 4). The results of the triple power-law fit show a break-up of $\Delta\gamma_{21} = -0.30$ at 49 keV and a break-down of $\Delta\gamma_{32} = 0.43$ at 134 keV. The break-up is again significant at the 95% confidence level (see Table 1). The two isothermal components and their temperatures are shown in Figure 4 in red and green. The high temperature is about 47 MK. The break-up is above the energies where thermal emission dominates.

- 3) Interval 5, 31-Oct-2002 16:51:15.65 to 16:51:23.95 UT.

After the peak, E_* is even higher (213 keV, although the uncertainty is large) and the spectrum is steeper ($\delta=4.62$) than at the peak (Figure 4). Therefore, only the break-up knee ($\Delta\gamma_{21} = -0.66$) can be seen at ~ 58 keV. The break-down is out of the range where the flux is above the background. The high temperature is about 45 MK for this interval.

In summary, the column density of fully ionized plasma N_* continued to increase during the HXR peak and the spectral index followed a soft-hard-soft time evolution. As a result, in the spectrum we see the break-up moved above the thermal energy range during interval 3 and continued moving to higher energies. The break-down also moved to higher energies and was presumably above the observable range in interval 5, the interval just after the peak. In intervals 3 and 4, we see clearly both the break-up and break-down features.

5. Discussion

There are many possible processes (Su et al. 2009), such as the acceleration process itself, directionality of the emission (Bai & Ramaty 1978) and albedo, that can produce a downward break with increasing photon energy in HXR flare spectra. However, there are few that produce an upward break. Compared with downward breaks, the upward break has been rarely reported (Dulk et al. 1992) and studied. Possible models are: 1) An additional thermal component at high temperature. 2) A combination of two or more nonthermal spectral components with different slopes (Li & Gan 2011). For example, the total spectrum may be the sum of spectra from two or more sources with different spectral indexes. Alternatively, it might result from the evolution of a single power-law spectrum during the integration time interval. 3) The acceleration mechanism might produce an

accelerated electron distribution with an upward break at low energies and/or a downward break at high energies. 4) Nonuniform ionization in the thick target region.

In our study, we already added a second isothermal component with a temperature of over 40 MK. But we still have the break-up in the spectra. An additional isothermal component with a temperature of 51, 71 and 89 MK would be needed for interval 3, 4 and 5, respectively, to explain the upward break. We also tried to use multi-thermal emission plus a power-law with a downward break to fit the spectra. A power-law temperature distribution with a high temperature cutoff of 36, 81, and 89 MK is needed for a good fit for the three intervals, respectively. We consider these temperatures to be unlikely, since there is no other evidence for such a high temperature component in solar flares. A study by Caspi (2010) indicates that the highest temperature found in GOES M1 to X10 class flares is ~ 50 MK. Even if a super hot component could be responsible for the upward breaks, it cannot explain the downward breaks and their time evolution.

We checked the spectra at shorter time intervals (~ 4 s). They showed similar spectral shapes. We also found no evidence for significantly different spectra from the two footpoints, but there is much uncertainty in the shape of the imaged spectra. The spectral shape could result from the acceleration mechanism, an interesting possibility, but NUI provides a simpler explanation.

For the upward break alone, it is hard to distinguish these models. It is possible that one mechanism caused one break and another mechanism gave the other. However, we find that the nonuniform ionization model is the only model that provides a simple and viable explanation for both the upward and downward breaks and their temporal evolution in this flare. The upward and downward breaks provide the first evidence for the full features of the spectrum expected from a nonuniformly ionized thick target. It suggests that high-energy electrons do penetrate into the deep atmosphere where the material is neutral, as expected in the collisional thick-target model. The time evolution of E_* indicates that a substantial volume of cool material was heated and ionized during the flare. Based on the average values of N_* , the ratio of N_* for intervals 1 and interval 6 indicates that 350 times the column density of ionized plasma in the rising phase of the flare was heated and became ionized. Considering the large uncertainties in N_* for these intervals, this factor is at least 25.

We did not consider return-current energy losses (Knight & Sturrock 1977; Emslie 1980; Zharkova & Gordovskyy 2006), the electron pitch-angle distribution and pitch-angle scattering (Petrosian 1973; Leach & Petrosian 1981; Diakonov & Somov 1988; Massone et al. 2004). Return-current losses flatten the spectra at low energies, which is inconsistent with the observed steepening of the spectra at these energies. Electrons with higher pitch angles

required a higher energy to reach the column density N_* . For a given value of E_* , higher pitch-angle electrons imply a smaller value for N_* . Therefore, the column densities of fully ionized plasma obtained here are an upper limit to those that would be deduced for electrons with higher pitch angles. A distribution of electron pitch angles broadens the flattened region above the E_* given by Equation 5. Our qualitative conclusions still hold, since the spectral shape and its time evolution support the NUI model. However, the pitch-angle distribution and pitch-angle diffusion will need to be considered in quantitative studies in the future. The dependence of Λ_{ee} and Λ_{eH} on electron energy and plasma properties will also need to be considered.

Our results for this flare support the collisional thick-target model in which the nonthermal electrons are accelerated in the corona and stream into the lower atmosphere. Notice that this flare was not selected through a random search for flares that particularly have upward breaks, but was selected because this was the most likely flare to show the expected upward break due to NUI. We expect to see more spectra of this type (spectra with upward breaks or with both upward and downward breaks) in other flares, especially after the HXR peak, since the plasma has been heated by nonthermal electrons and the column density of the ionized plasma (N_*) has significantly increased. We will continue to work on this flare with a detailed study to determine the density distribution in the flaring loop and the height at which the fractional ionization level changed from 1 to 0 and their time evolution.

We thank the *RHESSI* PI team for the excellence and easy availability of the data and the analysis software. Yang Su thanks Dr. Linhui Sui and Dr. Jeffrey W. Brosius for providing the research opportunity, Qingrong Chen and the referee for the valuable discussions and comments. Yang Su also acknowledges NSF support through ATM-0725135 and NASA support through grant NNX06AE64G. This work was supported in part by the National Natural Science Foundation of China (Grant Nos. 10773031, 10833007, 11078025), the Ministry of Science and Technology of China (MSTC 2011CB811402), the *RHESSI* Project, and a NASA HGI (Heliophysics Guest Investigator) grant.

Facilities: *RHESSI*.

REFERENCES

- Bai, T., & Ramaty, R. 1978, *ApJ*, 219, 705
- Brown, J. C. 1971, *Sol. Phys.*, 18, 489
- Brown, J. C. 1973, *Sol. Phys.*, 28, 151

- Brown, J. C., McArthur, G. K., Barrett, R. K., McIntosh, S. W., & Emslie, A. G. 1998, *Sol. Phys.*, 179, 379
- Caspi, A. 2010, Ph. D. Thesis, U.C. Berkeley
- Diakonov, S. V., & Somov, B. V. 1988, *Sol. Phys.*, 116, 119
- Dulk, G. A., Kiplinger, A. L., & Winglee, R. M. 1992, *ApJ*, 389, 756
- Emslie, A. G. 1978, *ApJ*, 224, 241
- Emslie, A. G. 1980, *ApJ*, 235, 1055
- Haug, E. 1997, *A&A*, 326, 417
- Holman, G. D. 2003, *ApJ*, 586, 606
- Koch, H. W., & Motz, J. W. 1959, *Reviews of Modern Physics*, 31, 920
- Knight, J. W., Sturrock, & P. A. 1977, *ApJ*, 218, 306
- Kontar, E. P., Brown, J. C., & McArthur, G. K. 2002, *Sol. Phys.*, 210, 419
- Kontar, E. P., Brown, J. C., Emslie, A. G., & Schwartz, R. A. 2003, *ApJ*, 595, 123
- Kontar, E. P. & Brown, J. C. 2006, *ApJ*, 653, 149
- Kontar, E. P., MacKinnon, A. L., Schwartz, R. A., & Brown, J. C. 2006, *A&A*, 446, 1157
- Leach, J., & Petrosian, V. 1981, *ApJ*, 251, 781
- Li, Y. P., & Gan, W. Q. 2011, *Sol. Phys.*, 269, 59
- Lin, R. P., Dennis, B. R., Hurford, G. J., et al. 2002, *Sol. Phys.*, 210, 3
- Massone, A. M., Emslie, A. G., Kontar, E. P., Piana, M., Prato, M., & Brown, J. C. 2004, *ApJ*, 613, 1233
- Petrosian, V. 1973, *ApJ*, 186, 291
- Smith, D. M., Lin, R. P., Turin, P., et al. 2002, *Sol. Phys.*, 210, 33
- Su, Y., Holman, G. D., Dennis, B. R., Tolbert, A. K., & Schwartz, R. A. 2009, *ApJ*, 705, 1584
- Zharkova, V. V., & Gordovskyy, M. 2006, *ApJ*, 651, 553

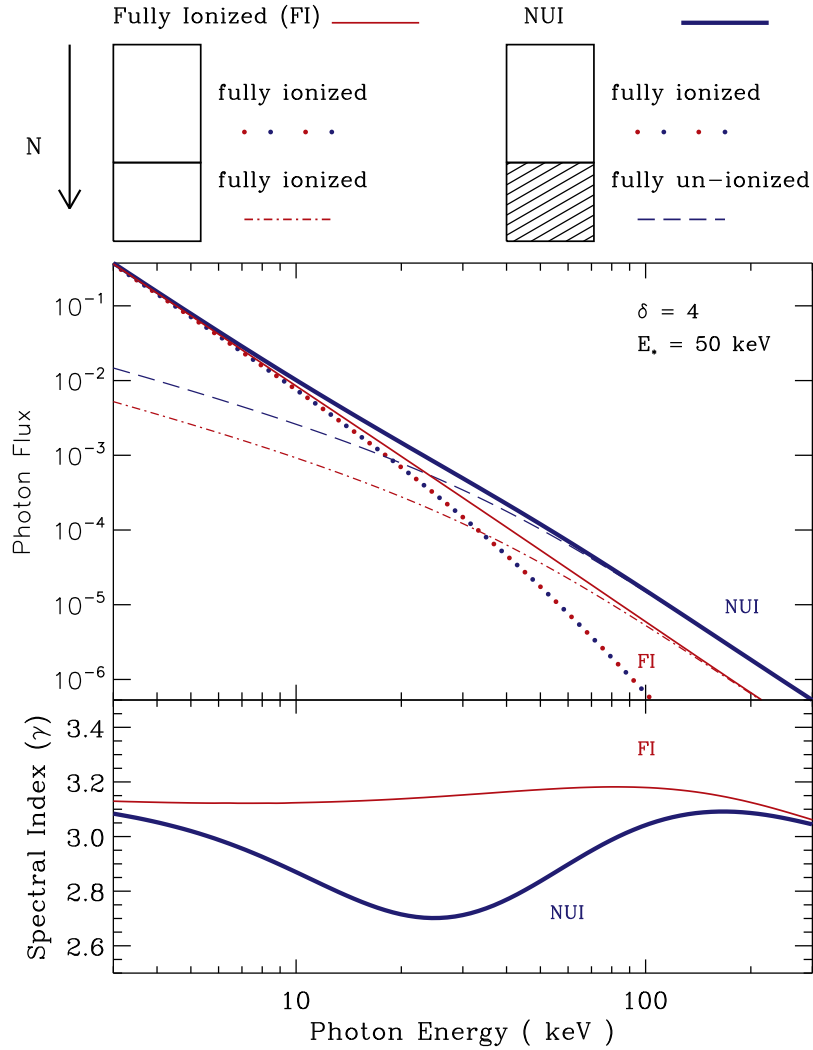


Fig. 1.— Comparison of photon spectra from a fully ionized (FI) thick target and a nonuniformly ionized (NUI) thick target with $E_* = 50$ keV for a power-law electron distribution with $\delta = 4$. The two models are illustrated in the *top panel* of the figure. *Middle panel:* The upper, thick solid blue line is the photon spectrum from NUI. The lower, thin solid red line is for the spectrum from a fully ionized thick target. The emission from the upper region (red-blue dotted line), where the plasma is fully ionized in both cases, is the same in the two models. The emission from the lower region in the NUI model (upper, dashed blue line) is 2.8 times higher than that in the fully ionized thick target (lower, dot-dashed red line). *Bottom panel:* the spectral index γ as a function of photon energy ε for the two models. See the color version in the electronic edition of *The Astrophysical Journal*.

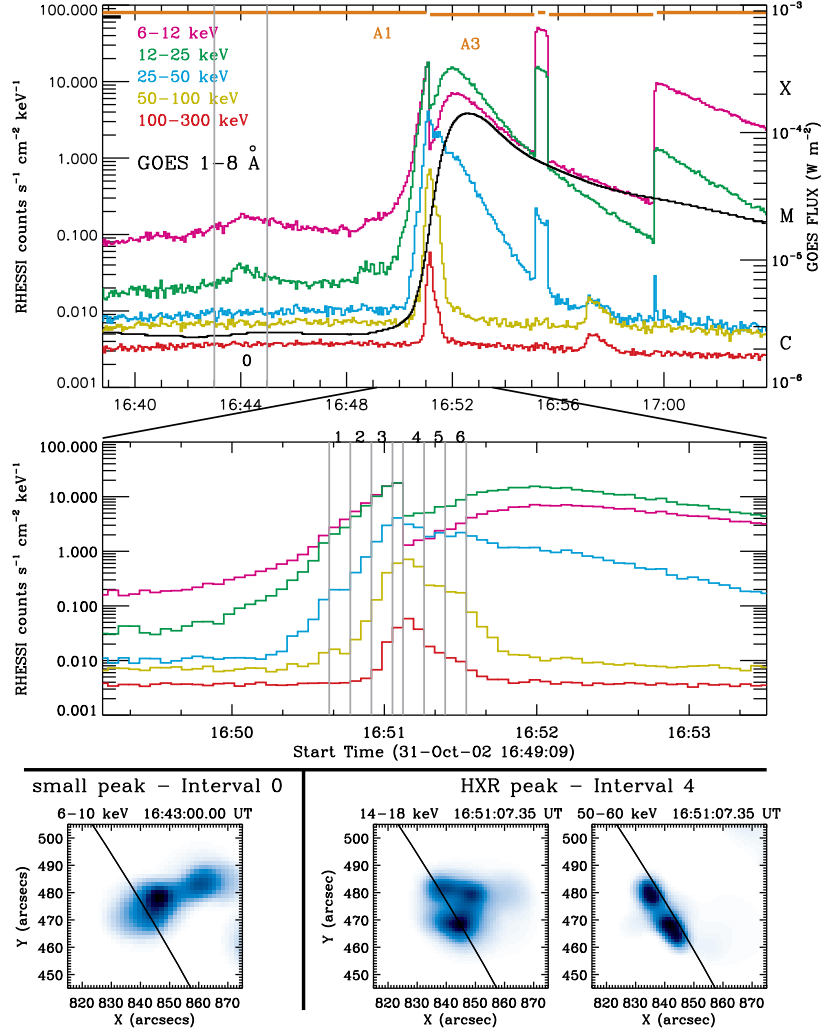


Fig. 2.— *Top panel:* GOES 1-8 Å and RHESSI light curves at different energies for the 31 October 2002 flare. The breaks in the light curves correspond to attenuator changes (A1⇒A3) during the RHESSI observations. The minor HXR peak at 16:57 UT, clearly visible above 50 keV, was due to particles. The vertical lines show the weak peak before the flare (interval 0). *Middle panel:* Magnification of the light curves around the peak time. The vertical lines show the six time intervals (1-6) we selected during the impulsive peak. *Bottom panel:* Pixon image at 6-10 keV for interval 0 (left) and at 14-18 keV (middle) and 50-60 keV (right) for interval 4.

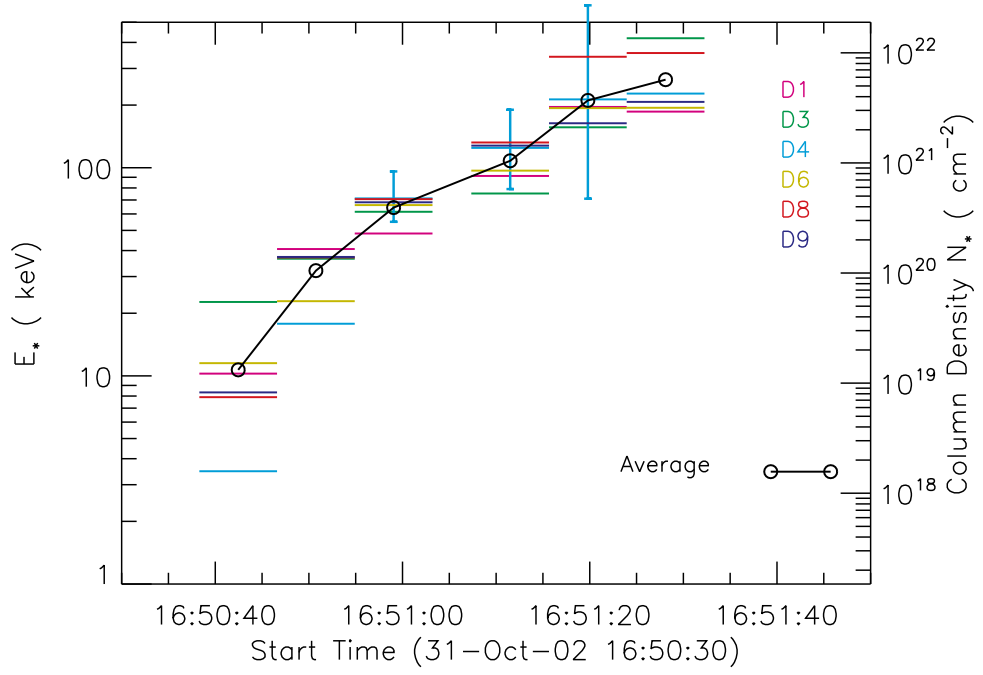


Fig. 3.— The time evolution of E_* and corresponding N_* for each of the six time intervals and RHESSI detectors examined. The circles show the average value of E_* for each time interval. The 95% confidence intervals determined from Monte Carlo simulation (~ 2 sigma) for E_* from detector 4 are also shown (vertical bars) for intervals 3, 4 and 5 for comparison with the spread in the results from the different detectors.

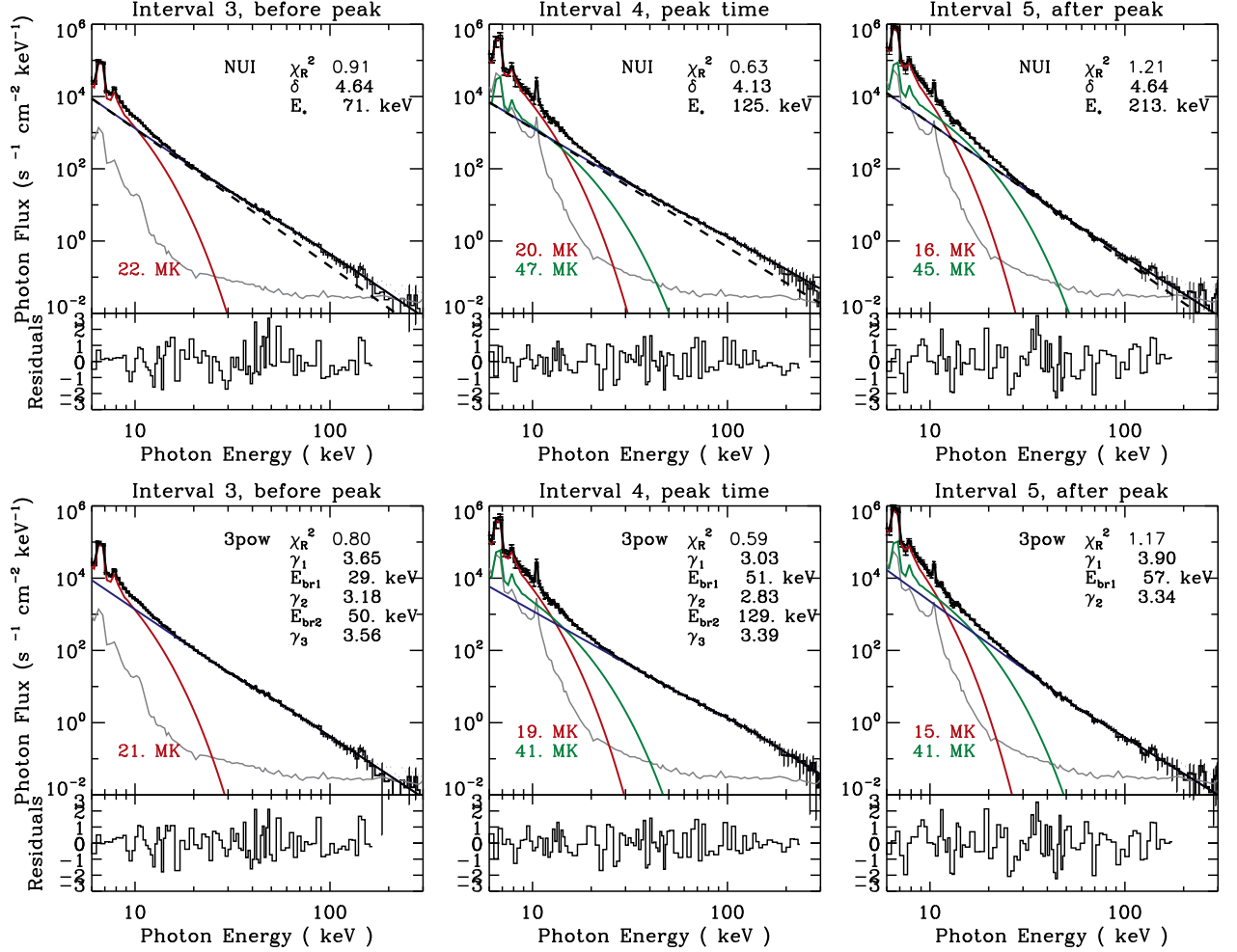


Fig. 4.— Both the NUI fit (top panels) and triple power-law fit (bottom panels) to the spectra of intervals 3, 4 and 5. The red and green lines show thermal components and the blue line shows the NUI or triple power-law nonthermal component. The blue dashed line shows the fully ionized thick-target spectrum from the same electron distribution as derived for the NUI model for comparison. The thin, solid gray line shows the background spectrum. Normalized residuals are shown below the spectra. An instrumental line at 10.5 keV was included when needed. All the derived parameters are shown for each fit in the plots, and in Table 1, with uncertainties.

Table 1. Fit parameters (most probable values) from detector 4 and 95% confidence intervals for time intervals 3, 4 and 5.

Function	Parameters	Interval 3		Interval 4		Interval 5	
NUI 95%	δ	4.64	(-0.06/+0.04)	4.12	(-0.07/+0.05)	4.62	(-0.11/+0.15)
NUI 95%	E_* (keV)	72	(-17 /+24)	125	(-46/+65)	213	(-142/+390)
Triple Power-law	γ_1	3.66	(-0.16/+0.21)	3.03	(-0.11/+0.32)	3.92	(-0.15/+0.24)
Triple Power-law	E_{bk1} (keV)	30	(-5/+7)	49	(-13/+38)	58	(-13/+18)
Triple Power-law	γ_2	3.16	(-0.66/+0.15)	2.81	(-0.58/+0.10)	3.33	(-0.27/+0.20)
Triple Power-law	E_{bk2} (keV)	49	(-10/+22)	134	(-52/+58)	—	—
Triple Power-law	γ_3	3.55	(-0.11/+0.25)	3.38	(-0.32/+2.58)	—	—
$\Delta\gamma_{21}$	$\gamma_2-\gamma_1$	-0.50	(-0.60/+0.24)	-0.30	(-0.6/+0.23)	-0.66	(-0.25/+0.30)
$\Delta\gamma_{32}$	$\gamma_3-\gamma_2$	0.37	(-0.20/+0.57)	0.43	(-0.31/+1.76)	—	—